nature structural & molecular biology

# Structural dynamics of potassium-channel gating revealed by single-molecule FRET

Shizhen Wang[1,5], Reza Vafabakhsh[2,5], William F Borschel[1], Taekjip Ha[2–4] & Colin G Nichols[1]

**Crystallography has provided invaluable insights regarding ion-channel selectivity and gating, but to advance understanding to a new level, dynamic views of channel structures within membranes are essential. We labeled tetrameric KirBac1.1 potassium channels with single donor and acceptor fluorophores at different sites and then examined structural dynamics within lipid membranes by single-molecule fluorescence resonance energy transfer (FRET). We found that the extracellular region is structurally rigid in both closed and open states, whereas the N-terminal slide helix undergoes marked conformational fluctuations. The cytoplasmic C-terminal domain fluctuates between two major structural states, both of which become less dynamic and move away from the pore axis and away from the membrane in closed channels. Our results reveal mobile and rigid conformations of functionally relevant KirBac1.1 channel motifs, implying similar dynamics for similar motifs in eukaryotic Kir channels and in cation channels in general.**



Because gated currents through single-ion-channel pores were first observed over 40 years ago[1], the gating behaviors of many ion channels have been recorded and analyzed at the single-molecule level, and numerous kinetic schemes have been developed to predict the physical states underlying gating transitions[2]. In addition, membrane-protein crystallography has provided high-resolution structures of ion channels in various configurations and has suggested conformational changes that must occur for currents to turn on and off[3–7]. Crystal structures have led to ideas regarding structural mobility and rigidity, such as: (i) the K-channel selectivity filter is a rigid structural feature[8–10]; (ii) the slide helix of inward rectifier potassium (Kir) channels[11–14], or the short α-helix that links the voltage sensor and the channel pore in voltage-gated channels, has a role in controlling the helix-bundle crossing (HBC) gate[15,16]; and (iii) the Kir-channel cytoplasmic domain itself moves relative to the transmembrane domain during gating[4,17,18]. However, crystallographic analyses cannot test these ideas because such methodologies typically access only a few stable states of channel proteins and do so in environments that are very different from the lipid bilayer. Hence, the relevance of crystallographic 'snapshots' to the dynamic gating events of ion channels in cell membranes may not always be apparent.

Kir channels have critical roles in shaping the action potentials of cardiomyocytes, potassium homeostasis of the kidney, hormone secretion of pancreatic β-cells, membrane potentials of nerve and glial cells, and the electrical activity of endothelial and smooth muscle cells[19]. Multiple Kir-channel structures have been resolved, but conformational trajectories of gating transitions remain speculative, although they are critical for a full understanding of gating mechanisms. KirBac1.1 is a prokaryotic Kir homolog that has the same core structural elements as eukaryotic Kir channels[17,20,21] and provides a model system to study Kir-channel gating; both crystallographic and molecular simulation analyses have indicated similar structures of open and closed channels in bacterial and eukaryotic Kir homologs[4,17,18,22]. Phosphatidylinositol 4,5-bisphosphate ($PIP_2$) is a gating ligand for many ion channels and is a universal activatory ligand for eukaryotic Kir channels[23–25], stabilizing the open conformation[4,17,19,25]. In prokaryotic KirBac1.1, the $PIP_2$-binding site is not identical to that in eukaryotic channels, thus resulting in a switched coupling whereby $PIP_2$ acts to stabilize the closed state[26].

Single-molecule FRET (smFRET) can report on unsynchronized conformational changes that are masked by ensemble averaging of macroscopic measurements[27,28], and it may bridge the gap between crystal structures and single-ion-channel current analyses. Very few membrane proteins have been studied by smFRET[29–33], owing to the technical challenges of position-specific fluorophore labeling, particularly in multimeric proteins. In the present study, we set out to analyze the dynamics of structural motions in KirBac1.1 in closed ($PIP_2$ bound) and open (ligand-free) states through smFRET. The results reveal both flexible and rigid motifs of the channel, confirming and refuting various previous ideas about structural mobility, and generating new ideas regarding the structural dynamics of the gating transition itself in potassium channels.

## RESULTS

### Labeled tetrameric KirBac1.1 for single-molecule imaging

In liposomes of defined composition (3:1 1-palmitoyl-2-oleoyl-*sn*-glycero-3-phosphoethanolamine) (POPE)/1-palmitoyl-2-oleoyl-*sn*-glycero-3-phosphoglycerol (POPG)) without $PIP_2$, KirBac1.1 channels

[1]Center for Investigation of Membrane Excitability Diseases, Department of Cell Biology and Physiology, Washington University School of Medicine, St. Louis, Missouri, USA. [2]Department of Physics, Center for the Physics of Living Cells, University of Illinois at Urbana-Champaign, Urbana, Illinois, USA. [3]Howard Hughes Medical Institute, Baltimore, Maryland, USA. [4]Department of Biophysics and Biophysical Chemistry, Johns Hopkins University, Baltimore, Maryland, USA. [5]These authors contributed equally to this work. Correspondence should be addressed to T.H. (tjha@jhu.edu) or C.G.N. (cnichols@wustl.edu).

Received 11 August; accepted 6 November; published online 7 December 2015; doi:10.1038/nsmb.3138

exhibited spontaneous bursts of openings, but the channels were essentially completely closed after incorporation of $PIP_2$ (**Fig. 1a**,**b** and **Supplementary Table 1**). In the absence of $PIP_2$, three distinct closed times were resolvable (**Fig. 1c**), and when open, the channels occupied two resolvable conductance levels (**Fig. 1b**) with similar durations. The mean probability of a channel being in any open state ($P_o$) was ~0.12 under control conditions but was reduced to ~0.004 in the presence of 5 μM $PIP_2$ (**Fig. 1d**).

We successfully applied smFRET to KirBac1.1 channels by engineering, expressing, labeling and reconstituting concatemeric proteins containing only two cysteines within the tetrameric channel (**Fig. 2a–c**). We collected tetramer fractions of Alexa Fluor 555– and Alexa Fluor 647 c2 maleimide–labeled KirBac1.1 mutants by size-exclusion chromatography (**Supplementary Fig. 1a**) and reconstituted them into liposomes (3:1 POPE/POPG). Functional assays confirmed that all labeled mutants retained channel activity and sensitivity to $PIP_2$ inhibition similar to those of wild type (WT) (**Supplementary Fig. 1b**). We performed single-molecule imaging with a prism-based total internal reflection fluorescence (TIRF) microscope[28] with time resolutions of 30 ms and 100 ms (**Fig. 2d**). We found that the mutant proteins were labeled very specifically, and over 95% of fluorescent spots arose from labeled KirBac1.1 cysteine mutants (**Fig. 2e** and **Supplementary Fig. 1c**).

## Structural rigidity of the extracellular region

The backbone structure of the selectivity-filter region is remarkably consistent in all available K-channel crystal structures[7,8,34], but whether this simply reflects a stable crystallographic configuration rather than a functionally relevant rigidity is unknown. Computational and experimental analyses[35] have suggested conformational coupling of the selectivity filter to the loop that extends outward. To provide direct visualization of structural dynamics in the extracellular selectivity-filter region (**Fig. 3a**), we labeled the residue T120C at the top of this loop in KirBac1.1. Individual smFRET trajectories revealed a remarkably stable FRET efficiency of ~0.8, without marked fluctuations or shifts when the channel was closed by saturating $PIP_2$ (**Fig. 3a**,**b**, **Supplementary Fig. 2a** and **Supplementary Table 2**). smFRET histograms and population contour plots obtained from 76 individual channel records in the absence of $PIP_2$ (and 91 in the presence of $PIP_2$) (**Fig. 3b** and data acquired at 30-ms time resolution in **Supplementary Fig. 3a**) confirmed that FRET efficiencies at this position had a very narrow distribution that did not differ between closed and open states. These experiments provide a time-resolved demonstration of the rigidity of the extracellular selectivity-filter region, independent of the channel gating state, in functional channels embedded within a lipid-membrane environment.

## Slide-helix constriction in $PIP_2$

A ubiquitous structural motif of many K channels, the N-terminal amphipathic slide helix, forms a 'belt' around the channel at the cytoplasmic face of the membrane and has been proposed to be a key linking element between ligand-binding or voltage-sensing gating domains and the pore[16,36]. In Kir channels, the slide helix may participate in controlling the HBC gate, but structural mechanisms are not clear[4,17,21,37,38]. We placed FRET pairs in dimeric constructs at opposing A45C residues located at the N-terminal ends of the slide helices (**Fig. 2a**,**b**). As shown by individual smFRET trajectories (**Fig. 3c** and **Supplementary Fig. 2b**), more than 50% of traces exhibited rapid fluctuations in FRET efficiencies between three major states in both the absence and the presence of $PIP_2$. The dimensionless variance in fluorescence intensities of singly (Alexa Fluor 555) labeled A45C–WT (8.7 ± 1.7) and T120C–WT (5.7 ± 1.2) samples were not significantly different, results consistent with the measured FRET changes at residue 45 resulting from conformational changes rather than changes in signal-to-noise ratio or changes in local quantum efficiency.

smFRET contour plots and histograms from 121 individual recordings in the absence of $PIP_2$ (139 with $PIP_2$) (**Fig. 3d** and **Supplementary Fig. 2b**) revealed a distribution of FRET efficiencies between ~0.45 and ~0.95, suggesting a motion range of up to 20 Å between diagonally opposed slide helices (on the basis of distances ($r$) calculated with the Förster equation: $r = R_0 \times (1/E - 1)^{1/6}$, where $E$ is the FRET efficiency, and $R_0$ is the Förster distance of the Alexa Fluor 555 and Alexa Fluor 647 FRET pair (5.1 nm), with the assumption that the fluorophores can freely rotate at the labeling site; i.e, $\kappa^2 = 2/3$). The FRET efficiency distributions were well fit by the sum of three Gaussians (**Fig. 3d**, **Table 1** and **Supplementary Table 2**) without substantial alteration in the histogram peak positions, both with and without $PIP_2$. In the closed channel, individual trajectories (**Fig. 2c** and **Supplementary Fig. 2b**), as well as histograms (**Fig. 2d**), revealed

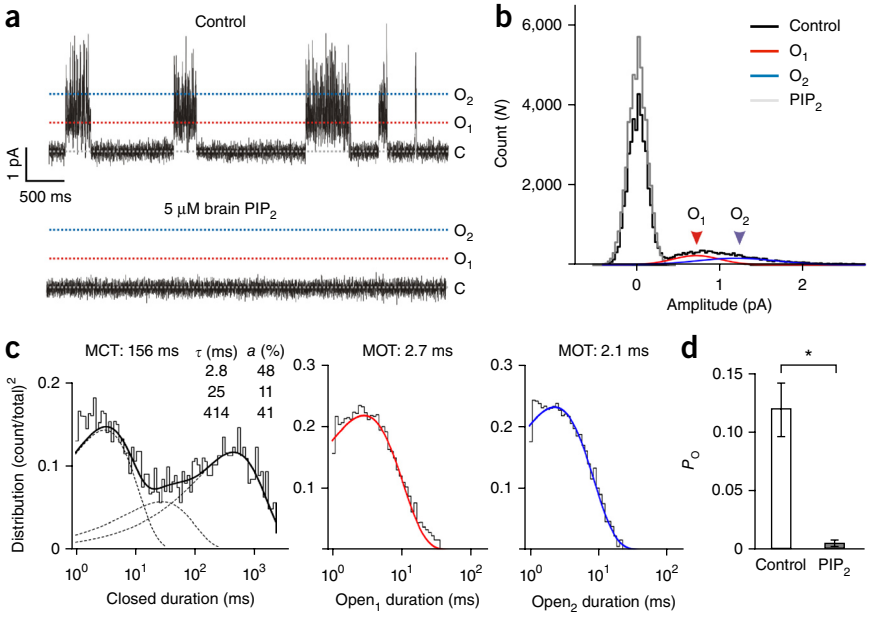


**Figure 1** $PIP_2$-dependent gating of KirBac1.1-channel activity. (**a**) Excised single-channel current traces of purified KirBac1.1 reconstituted into giant liposomes, before and after application of $PIP_2$. Two open (O1, O2) and closed (C) levels are indicated, (**b**) Amplitude histogram of the corresponding traces in **a** before (black) and after (gray) application of $PIP_2$. $N$, number of counts. (**c**) Closed and open interval distributions from the recording depicted in **a**, before application of $PIP_2$. Histograms are overlaid with the probability density function (thick lines) and individual exponential components (dotted lines). Mean closed time (MCT) and mean open time (MOT), time constants ($\tau$, ms) and corresponding areas ($a$, %) were calculated from fits to a model consisting of three closed states and one open state for each conductance class. (**d**) Open probability ($P_o$, mean ± s.e.m.) in the absence (0.12 ± 0.02, $n = 5$ patches) and presence (0.004 ± 0.002, $n = 3$) of $PIP_2$. *$P < 0.05$ by two-tailed Student's $t$ test).

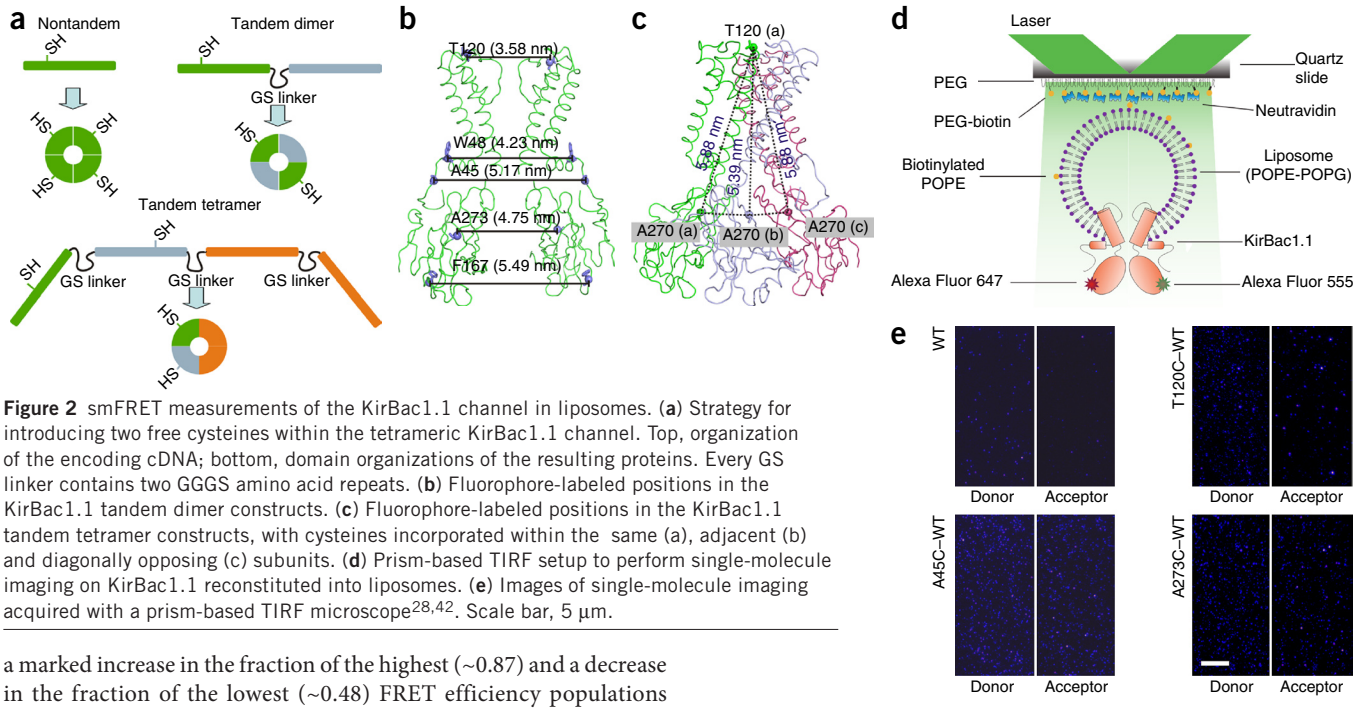


**Figure 2** smFRET measurements of the KirBac1.1 channel in liposomes. (**a**) Strategy for introducing two free cysteines within the tetrameric KirBac1.1 channel. Top, organization of the encoding cDNA; bottom, domain organizations of the resulting proteins. Every GS linker contains two GGGS amino acid repeats. (**b**) Fluorophore-labeled positions in the KirBac1.1 tandem dimer constructs. (**c**) Fluorophore-labeled positions in the KirBac1.1 tandem tetramer constructs, with cysteines incorporated within the same (a), adjacent (b) and diagonally opposing (c) subunits. (**d**) Prism-based TIRF setup to perform single-molecule imaging on KirBac1.1 reconstituted into liposomes. (**e**) Images of single-molecule imaging acquired with a prism-based TIRF microscope[28,42]. Scale bar, 5 µm.

a marked increase in the fraction of the highest (~0.87) and a decrease in the fraction of the lowest (~0.48) FRET efficiency populations (**Table 1** and **Supplementary Table 2**). If we make the simplistic assumption that channel opening requires both diagonally opposed A45C pairs to be in the most dilated conformation (FRET efficiency ~0.48), the predicted open probability would be the square of the occupancy of the $P_{0.48}$ state, i.e., 0.13 ($0.36^2$) in the absence of $PIP_2$ and 0.04 ($0.20^2$) in the presence of $PIP_2$. These values were quite similar to the measured open probabilities (0.12 and 0.005, respectively; **Fig. 1d**), but further work will be necessary to validate these ideas.

Independent sets of A45C–WT smFRET data collected at 30-ms resolution generated very similar distributions and recapitulated the effects of $PIP_2$ on FRET distributions (**Supplementary Fig. 3a**). Although the shorter inter-residue distance reduced the sensitivity of the Alexa Fluor 555–Alexa Fluor 647 pair, we also observed qualitatively similar gating-dependent FRET changes in data from W48C–WT, located in the middle of the slide helix (**Supplementary Fig. 3b**). Our results thus implicate slide-helix motions during channel gating and suggest that closure of the channel involves tightening of the slide-helix belt, such that the lowest FRET states correspond to the 'dilated' belt that permits channel opening.

### Structural transitions in the C-terminal domain

Kir channels have a large C-terminal domain (CTD) with which many intracellular regulatory ligands interact[24]. We have previously reported reduced ensemble FRET efficiency at the A273C position in the presence of $PIP_2$ (ref. 22). In the present study, we again labeled two cytoplasmic-domain cysteines, F167C and A273C, as well as the external residue T120C with 5-((2-aminoethyl)amino)naphthalene-1-sulfonic acid (EDANS) and DABCYL Plus or Alexa Fluor 488 and QSY-7 FRET pairs in dimeric or tetrameric constructs, and we then measured the $PIP_2$-induced changes with ensemble FRET. Both 167C and 273C exhibited reduced FRET efficiencies with $PIP_2$, whereas we again observed no significant change in FRET efficiency at 120C (**Supplementary Fig. 4a**).

To visualize conformational dynamics of the CTD in closed and open states, we labeled diagonally opposed cysteines in the dimeric A273C–WT or F167C–WT constructs with Alexa Fluor 555 and Alexa Fluor 647 (**Fig. 2a**,**b**). As indicated by individual smFRET trajectories (**Fig. 3e** and **Supplementary Fig. 2c**), more than 60% of A273–WT traces exhibited fluctuations between two major conformations with mean FRET efficiencies of 0.74 and 0.41 in the absence of $PIP_2$. In the presence of saturating $PIP_2$, the number of traces showing detectable dynamic changes decreased to ~30% (**Fig. 3e** and **Table 2**), and both FRET peaks shifted toward lower FRET values of 0.68 and 0.32, respectively (**Fig. 3f**). These results are consistent with the ensemble FRET measurements but further suggest that the β-sheet containing residue 273 actually fluctuates between two major conformations, whether the channel is closed or open, and that both conformations are widened when the channel is closed. At the F167 site, the smFRET distributions also exhibited two clear peaks in both the absence and presence of $PIP_2$, and again induced only a slight shift toward lower FRET efficiency (**Supplementary Fig. 3b**). These data suggest that in addition to overall dilation in the closed channel, the major β-sheet in the CTD may undergo gating-independent 'breathing' conformational transitions that are not revealed in crystal structures.

### C-terminal displacement from the membrane in closed channels

Crystal structures of both potassium and sodium channels indicate that bending and rotation motions of the pore-forming transmembrane helices (TM2 or S6) are required to remove HBC gates[6,7,36,39]. For Kir channels, a rigidly coupled tilting or twisting of the CTD has also been proposed[4,18,22]. To test this idea directly, we constructed three concatemeric tetramers in which the channels were labeled across the membrane, at one cysteine in the selectivity-filter region of the extracellular side (T120C) and at A270C in the CTD of the same, the neighboring or the diagonally opposed subunit (**Figs. 2c** and **4a**,**c**).

**Table 1 FRET populations at the A45C position from Gaussian fittings**

| A45C–WT | | $F_{0.87}$ | $F_{0.70}$ | $F_{0.48}$ | $P_o$ |
|---|---|---|---|---|---|
| Control | 100 ms | 0.21 | 0.43 | 0.36 | 0.12 |
| | 30 ms | 0.23 | 0.41 | 0.36 | |
| $PIP_2$ | 100 ms | 0.34 | 0.44 | 0.22 | 0.004 |
| | 30 ms | 0.36 | 0.44 | 0.20 | |

$F_x$, fraction of FRET distribution at efficiency = $x$. $P_o$, channel open probability.

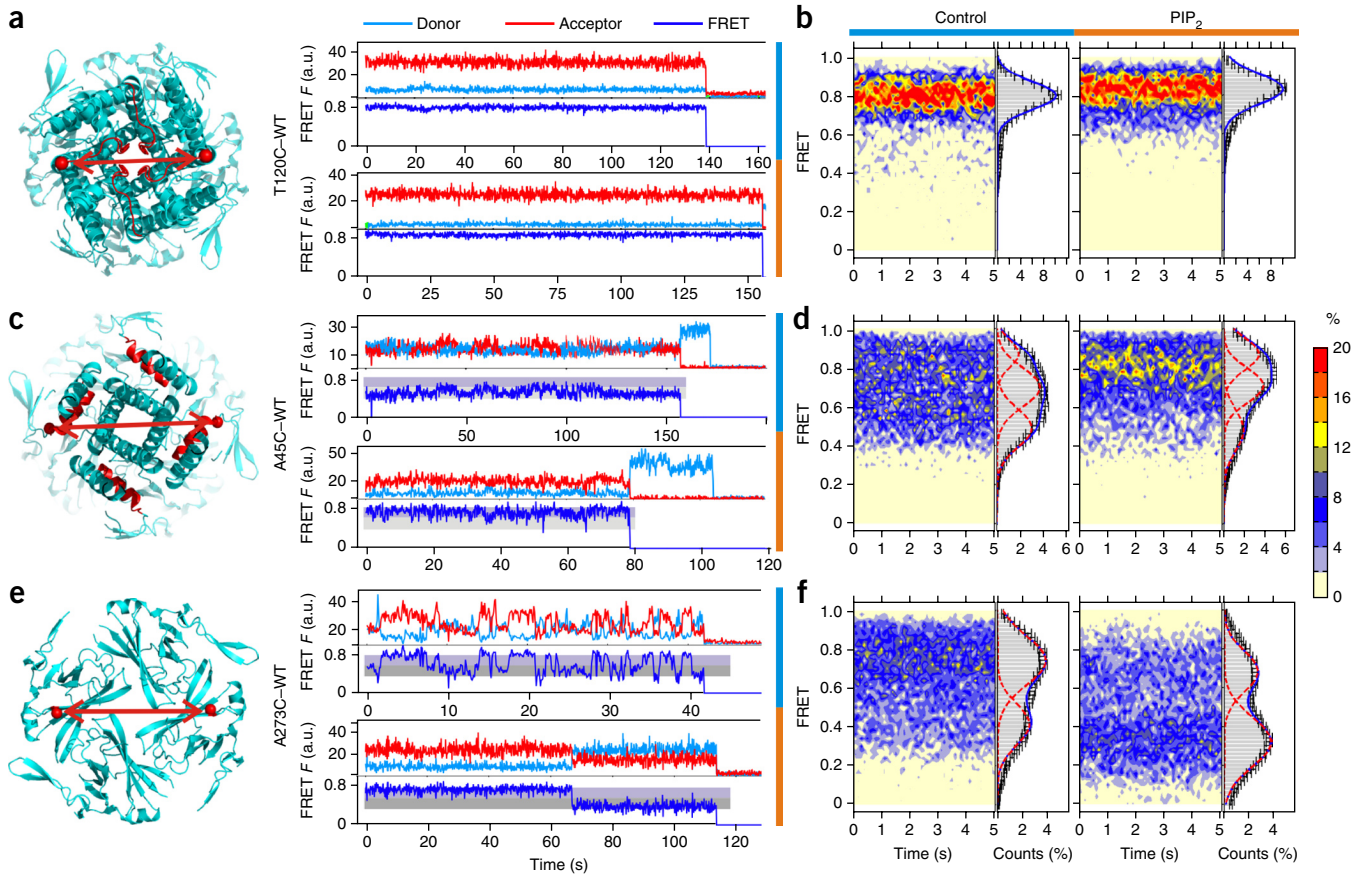


**Figure 3** Conformational fluctuations of KirBac1.1 in liposomes. (**a**–**f**) Labeling locations and representative smFRET traces for residues T120C (**a**), A45C (**c**) and A273F (**e**), as well as FRET contour plots and histograms (**b**,**d** and **f**; mean ± s.e.m. ($n$ = 76 and 91 T120 traces, 121 and 139 A45C traces, and 175 and 204 A273C traces in the absence or presence of $PIP_2$, respectively)) of KirBac1.1 in liposomes with (red bars) or without (blue bars) $PIP_2$. *F*, fluorescence; a.u., arbitrary units.



smFRET trajectories, as well as FRET contour plots and histograms from these three constructs, all indicated a shift to decreased FRET efficiencies when the channels were closed by $PIP_2$ (**Fig. 4** and **Supplementary Fig. 5**). Ensemble FRET data from the same constructs were again consistent with those calculated from smFRET measurements (**Supplementary Fig. 4b**). These data thus indicate that the CTD indeed moves away from the transmembrane domain (TM) when the channel closes; the FRET efficiencies were consistent with the channel being ~80 Å long in the closed state, a length similar to the channel length observed in the 1P7B KirBac1.1 crystal structure[21], and becoming ~10 Å shorter in the open state. This conclusion is consistent with those of other crystallographic and simulation studies[17,40], but the data do not support gating being associated with a major twisting motion of the CTD relative to the TM[41], because such a motion would differentially affect the FRET signals in the three intra- or intersubunit arrangements.

### Relating structural dynamics to ion-current gating

At location T120C in the extracellular portion of the channel near the selectivity filter, there was little detectable dynamics; over 90% of traces showed no change in FRET efficiency before donor or acceptor photobleaching (**Table 2**), and we detected no cross-correlation between donor and acceptor signal (**Fig. 5a**). In contrast, A45C in the slide-helix region exhibited a strong donor-acceptor cross-correlation with a decay time constant that was not dramatically altered by $PIP_2$ (**Fig. 5b**). We propose that the structural dynamics at A45C is dominated by transitions among the multiple conformations of the closed state and that channel opening may occur at the lowest FRET conformations (**Fig. 3c**,**d**). At the nearby residue W48C, the FRET signals were less dynamic (**Supplementary Fig. 3b**), a result that may be a consequence of each residue being located in different secondary structures or different local environments (i.e, A45 is located just before the slide helix

**Table 2 Effect of $PIP_2$ on the structural dynamics of KirBac1.1 evaluated by cross-correlation analysis[a]**

| | | $a_1$ (%) | $\tau_1$ (ms) | $a_2$ (%) | $\tau_2$ (ms) | Dynamic traces[b] |
|---|---|---|---|---|---|---|
| T120C–WT | Control | | | | | 0.09 |
| | $PIP_2$ | – | – | – | – | 0.03 |
| A45C–WT | Control | 69.7 | 111 | 92.0 | 1,595 | 0.55 |
| | $PIP_2$ | 78.1 | 94 | 120 | 1,017 | 0.64 |
| A273C–WT | Control | 73.7 | 75.5 | 146 | 1,176 | 0.60 |
| | $PIP_2$ | 17.7 | 238 | 63.9 | 1,966 | 0.33 |

[a]The cross-correlation analysis was performed with the algorithm $C_{auto}(t) = \langle \Delta FRET_0 \Delta FRET_t \rangle / \langle \Delta FRET_0^2 \rangle$, where $\Delta FRET_0$ and $\Delta FRET_t$ are the variances of FRET efficiencies at times 0 and $t$, respectively. The cross-correlation analysis was performed with the algorithm $C_{cross}(t) = \langle \Delta Fd_0 \Delta Fa_t \rangle / \langle \Delta Fd_0 \Delta Fa_0 \rangle$, where $\Delta Fd_0$, $\Delta Fa_0$ and $\Delta Fa_t$ are variances of donor and acceptor fluorescence at times 0 and $t$, respectively. All lag times ($t$) versus coefficients from cross covariance analyses were fitted with either single- or two-component exponential functions, $f(C_{auto}, t) = a_1 e^{-\frac{1}{\tau 1}} + a_2 e^{-\frac{1}{\tau 2}}$ or $f(C_{auto}, t) = a_1 e^{-\frac{1}{\tau 1}}$.

[b]The FRET efficiency histogram of any trace exhibiting more than one population was arbitrarily defined as dynamic, in order to provide a semiquantitative assessment of the dynamic behaviors of the labeled structural motifs.

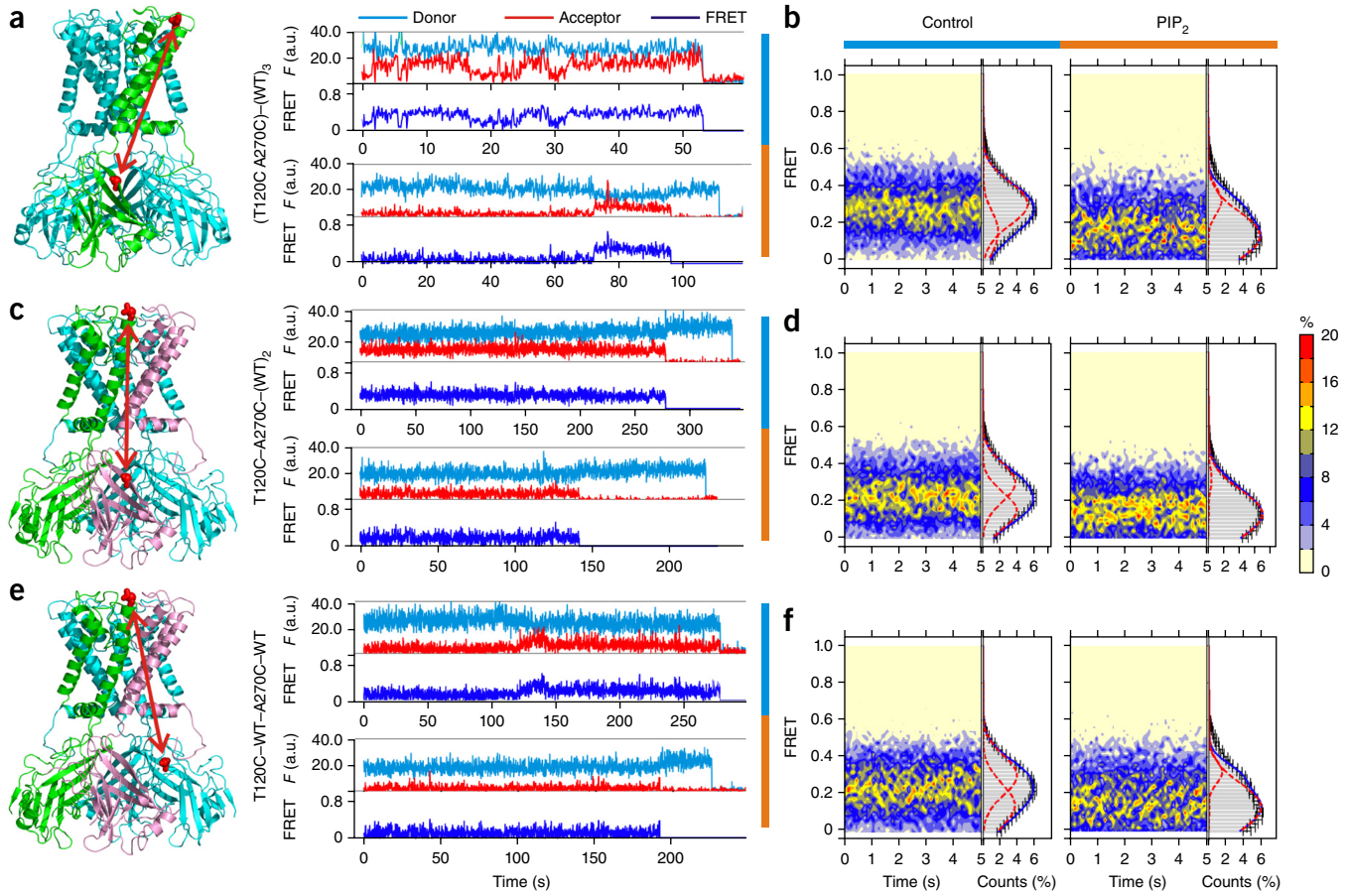


**Figure 4** Motion of the TM with respect to CTD upon $PIP_2$ gating. (**a**–**f**) Labeling locations and representative smFRET traces for T120C-A270C residue pairs, with A270C located in the same subunit (**a**), the clockwise preceding residue (**c**) or the diagonally opposite subunit (**e**) relative to T120C, as well as FRET contour plots and histograms (**b**,**d** and **f**) of KirBac1.1 in liposomes with (orange bars) or without $PIP_2$ (blue bars) (mean ± s.e.m. ($n$ = 267 (**b**), 222 (**d**) and 182 (**f**) traces in control, and 160 (**b**), 211 (**d**) and 149 (**f**) traces in $PIP_2$).

in a loop interacting with the CTD and is relatively more exposed to the cytoplasm, whereas W48 constitutes part of the slide helix itself and sits at the cytoplasm-membrane interfacial region). We observed striking differences in FRET dynamics between active and closed channels at residue A273 of the CTD (**Figs. 3e** and **5c**). The donor-acceptor cross-correlation of the A273C–WT sample was well fit with a double exponential function, with both time constants substantially increasing in $PIP_2$ while the amplitude of both components decreases (**Fig. 5c**). These changes suggest that the frequency of the conformational fluctuations in this region is suppressed when the channel is closed, consistently with a model in which ion-current gating at the HBC is directly coupled to conformational changes in the CTD[22].

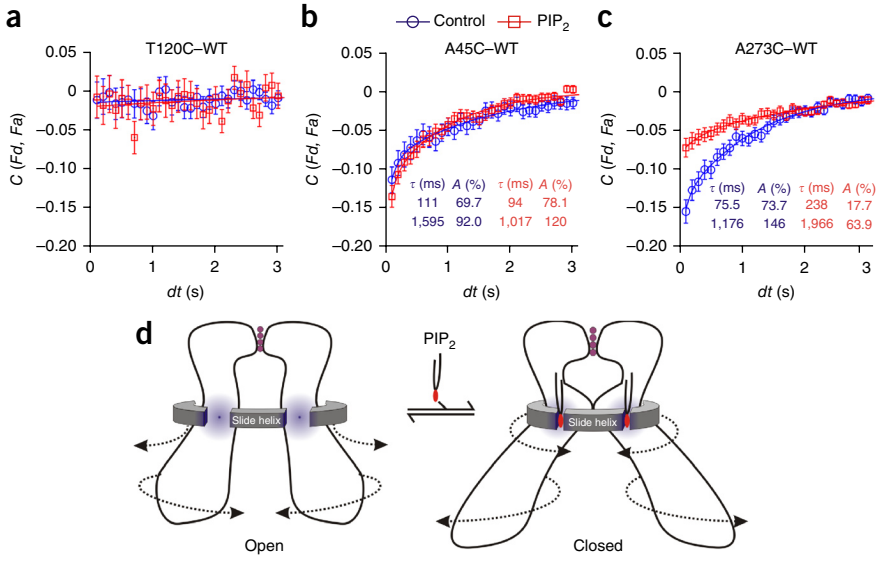


**Figure 5** Conformational dynamics of KirBac1.1- and $PIP_2$-dependent gating. (**a**–**c**) Cross-correlation ($C$) of donor ($Fd$) and acceptor ($Fa$) fluorescence traces of KirBac1.1 mutants with fluorophore labeling at T120C near the selectivity filter versus time ($dt$). (**a**), A45C in the slide helix (**b**) or A273C in the CTD (**c**), in the absence and presence of $PIP_2$ (mean ± s.e.m., $n$ = 79 (**a**), 121 (**b**) and 175 (**c**) traces in control, and 90 (**a**), 139 (**b**) and 204 (**c**) traces in $PIP_2$). Fitted time constant ($\tau$) and amplitude ($A$) are indicated in each case. (**d**) Proposed motions underlying gating of the KirBac1.1 channel. $PIP_2$ binds at the TM-CTD interface and tightens the slide-helix belt and confines the channel-pore opening. Tilting or twisting motions of the CTD couple to the HBC-gate closure, slowing down structural fluctuations of the CTD.

## DISCUSSION

Crystal structures provide images of channels in distinct states but cannot reveal the connectivity between states or provide time trajectories of structural changes. Our detection of unsynchronized structural dynamics with smFRET provides a view of the intramolecular motions that underlie Kir-channel function within lipid membranes.

Certain findings are quite striking and may have substantial implications for other channels. Perhaps most notably, the external selectivity-filter region exhibits no detectable structural fluctuations, thus demonstrating a rigidity that may be necessary to maintain ion selectivity of the pore. In contrast, both the slide helix and the CTD show marked structural dynamics and structural flexibility. Our results suggest that the tightness of the slide-helix belt controls channel gating (**Fig. 5d**). In KirBac1.1 the belt is tightened by $PIP_2$ binding, a structural consequence that may be reversed for eukaryotic Kir channels in which a structurally distinct slide helix is involved in $PIP_2$-dependent activation[17]. The motions that we detected in the KirBac1.1 slide helix and CTD reflect a marked intrinsic flexibility of the channel structure. As more ion channels become amenable to approaches similar to those described here, the conformational changes induced by gating processes in eukaryotic Kir and other ion channels may be revealed to be more dramatic and more complex than currently perceived.

## METHODS

Methods and any associated references are available in the online version of the paper.

*Note: Any Supplementary Information and Source Data files are available in the online version of the paper.*

### ACKNOWLEDGMENTS

Financial support was provided by US National Institutes of Health (NIH) grant HL54171 (C.G.N.) and US National Science Foundation grant PHY1430124 (T.H.). T.H. is supported as an investigator of the Howard Hughes Medical Institute. W.F.B. was supported by NIH grants T32 HL007275 and T32 HL125241.

### AUTHOR CONTRIBUTIONS

S.W., R.V., T.H. and C.G.N. conceived and designed the experiments; S.W. and W.F.B. performed the electrophysiological studies; S.W. designed, constructed, purified and labeled the protein samples with fluorophore; W.F.B. analyzed the single-channel recordings; and S.W. and R.V. collected and analyzed the smFRET data. The paper was written by S.W. and C.G.N. and edited by R.V., W.F.B. and T.H.

### COMPETING FINANCIAL INTERESTS

The authors declare no competing financial interests.



1. Neher, E. & Sakmann, B. Single-channel currents recorded from membrane of denervated frog muscle fibres. *Nature* **260**, 799–802 (1976).
2. Colquhoun, D. & Sigworth, F. in *Single-channel Recording* 483–587 (Springer, 1995).
3. Cao, E., Liao, M., Cheng, Y. & Julius, D. TRPV1 structures in distinct conformations reveal activation mechanisms. *Nature* **504**, 113–118 (2013).
4. Whorton, M.R. & MacKinnon, R. Crystal structure of the mammalian GIRK2 K+ channel and gating regulation by G proteins, PIP2, and sodium. *Cell* **147**, 199–208 (2011).
5. Cuello, L.G., Jogini, V., Cortes, D.M. & Perozo, E. Structural mechanism of C-type inactivation in K+ channels. *Nature* **466**, 203–208 (2010).
6. Cuello, L.G. *et al.* Structural basis for the coupling between activation and inactivation gates in K+ channels. *Nature* **466**, 272–275 (2010).
7. Jiang, Y. *et al.* Crystal structure and mechanism of a calcium-gated potassium channel. *Nature* **417**, 515–522 (2002).
8. Zhou, Y., Morais-Cabral, J.H., Kaufman, A. & MacKinnon, R. Chemistry of ion coordination and hydration revealed by a K+ channel–Fab complex at 2.0 A resolution. *Nature* **414**, 43–48 (2001).
9. Nordengren, J. *et al.* Differential localization and expression of urokinase plasminogen activator (uPA), its receptor (uPAR), and its inhibitor (PAI-1) mRNA and protein in endometrial tissue during the menstrual cycle. *Mol. Hum. Reprod.* **10**, 655–663 (2004).
10. Bernèche, S. & Roux, B. Energetics of ion conduction through the K+ channel. *Nature* **414**, 73–77 (2001).
11. Nichols, C.G. KATP channels as molecular sensors of cellular metabolism. *Nature* **440**, 470–476 (2006).
12. Enkvetchakul, D., Jeliazkova, I., Bhattacharyya, J. & Nichols, C.G. Control of inward rectifier K channel activity by lipid tethering of cytoplasmic domains. *J. Gen. Physiol.* **130**, 329–334 (2007).
13. Männikkö, R. *et al.* Interaction between mutations in the slide helix of Kir6.2 associated with neonatal diabetes and neurological symptoms. *Hum. Mol. Genet.* **19**, 963–972 (2010).
14. Kuo, A., Domene, C., Johnson, L.N., Doyle, D.A. & Vénien-Bryan, C. Two different conformational states of the KirBac3.1 potassium channel revealed by electron crystallography. *Structure* **13**, 1463–1472 (2005).
15. Lu, Z., Klem, A.M. & Ramu, Y. Coupling between voltage sensors and activation gate in voltage-gated K+ channels. *J. Gen. Physiol.* **120**, 663–676 (2002).
16. Long, S.B., Campbell, E.B. & Mackinnon, R. Voltage sensor of Kv1.2: structural basis of electromechanical coupling. *Science* **309**, 903–908 (2005).
17. Hansen, S.B., Tao, X. & MacKinnon, R. Structural basis of $PIP_2$ activation of the classical inward rectifier K+ channel Kir2.2. *Nature* **477**, 495–498 (2011).
18. Bavro, V.N. *et al.* Structure of a KirBac potassium channel with an open bundle crossing indicates a mechanism of channel gating. *Nat. Struct. Mol. Biol.* **19**, 158–163 (2012).
19. Hibino, H. *et al.* Inwardly rectifying potassium channels: their structure, function, and physiological roles. *Physiol. Rev.* **90**, 291–366 (2010).
20. Cheng, W.W., Enkvetchakul, D. & Nichols, C.G. KirBac1.1: it's an inward rectifying potassium channel. *J. Gen. Physiol.* **133**, 295–305 (2009).
21. Kuo, A. *et al.* Crystal structure of the potassium channel KirBac1.1 in the closed state. *Science* **300**, 1922–1926 (2003).
22. Wang, S., Lee, S.J., Heyman, S., Enkvetchakul, D. & Nichols, C.G. Structural rearrangements underlying ligand-gating in Kir channels. *Nat. Commun.* **3**, 617 (2012).
23. Suh, B.C. & Hille, B. PIP2 is a necessary cofactor for ion channel function: how and why? *Annu. Rev. Biophys.* **37**, 175–195 (2008).
24. Xie, L.H., John, S.A., Ribalet, B. & Weiss, J.N. Activation of inwardly rectifying potassium (Kir) channels by phosphatidylinositol-4,5-bisphosphate (PIP2): interaction with other regulatory ligands. *Prog. Biophys. Mol. Biol.* **94**, 320–335 (2007).
25. Logothetis, D.E., Jin, T., Lupyan, D. & Rosenhouse-Dantsker, A. Phosphoinositide-mediated gating of inwardly rectifying K(+) channels. *Pflugers Arch.* **455**, 83–95 (2007).
26. Enkvetchakul, D., Jeliazkova, I. & Nichols, C.G. Direct modulation of Kir channel gating by membrane phosphatidylinositol 4,5-bisphosphate. *J. Biol. Chem.* **280**, 35785–35788 (2005).
27. Ha, T. *et al.* Probing the interaction between two single molecules: fluorescence resonance energy transfer between a single donor and a single acceptor. *Proc. Natl. Acad. Sci. USA* **93**, 6264–6268 (1996).
28. Roy, R., Hohng, S. & Ha, T. A practical guide to single-molecule FRET. *Nat. Methods* **5**, 507–516 (2008).
29. Zhao, Y. *et al.* Single-molecule dynamics of gating in a neurotransmitter transporter homologue. *Nature* **465**, 188–193 (2010).
30. Akyuz, N., Altman, R.B., Blanchard, S.C. & Boudker, O. Transport dynamics in a glutamate transporter homologue. *Nature* **502**, 114–118 (2013).
31. Erkens, G.B., Hänelt, I., Goudsmits, J.M., Slotboom, D.J. & van Oijen, A.M. Unsynchronised subunit motion in single trimeric sodium-coupled aspartate transporters. *Nature* **502**, 119–123 (2013).
32. Wang, Y. *et al.* Single molecule FRET reveals pore size and opening mechanism of a mechano-sensitive ion channel. *eLife* **3**, e01834 (2014).
33. Vafabakhsh, R., Levitz, J. & Isacoff, E.Y. Conformational dynamics of a class C G-protein-coupled receptor. *Nature* **524**, 497–501 (2015).
34. Roux, B. Ion conduction and selectivity in K(+) channels. *Annu. Rev. Biophys. Biomol. Struct.* **34**, 153–171 (2005).
35. Raghuraman, H., Islam, S.M., Mukherjee, S., Roux, B. & Perozo, E. Dynamics transitions at the outer vestibule of the KcsA potassium channel during gating. *Proc. Natl. Acad. Sci. USA* **111**, 1831–1836 (2014).
36. Payandeh, J., Scheuer, T., Zheng, N. & Catterall, W.A. The crystal structure of a voltage-gated sodium channel. *Nature* **475**, 353–358 (2011).
37. Xiao, J., Zhen, X.G. & Yang, J. Localization of PIP2 activation gate in inward rectifier K+ channels. *Nat. Neurosci.* **6**, 811–818 (2003).
38. Lee, S.J. *et al.* Secondary anionic phospholipid binding site and gating mechanism in Kir2.1 inward rectifier channels. *Nat. Commun.* **4**, 2786 (2013).
39. McCusker, E.C. *et al.* Structure of a bacterial voltage-gated sodium channel pore reveals mechanisms of opening and closing. *Nat. Commun.* **3**, 1102 (2012).
40. Bollepalli, M.K. *et al.* State-dependent network connectivity determines gating in a K+ channel. *Structure* **22**, 1037–1046 (2014).
41. Clarke, O.B. *et al.* Domain reorientation and rotation of an intracellular assembly regulate conduction in Kir potassium channels. *Cell* **141**, 1018–1029 (2010).
42. Joo, C. & Ha, T. Prism-type total internal reflection microscopy for single-molecule FRET. *Cold Spring Harb. Protoc.* **2012** Pdb.prot072041 (2012).

## ONLINE METHODS

**DNA manipulation.** KirBac1.1 WT cDNA was inserted between the NcoI and HindIII sites of the pQE60 vector[43]. For tandem dimer constructs, two copies of KirBac1.1 cDNA were inserted between the NcoI and BamHI, and the BamHI and HindIII sites, respectively. A short GGGSGGGS linker was introduced between the two copies of KirBac1.1 coding DNA. To make tandem tetramer constructs, two copies of tandem dimer–encoding DNA were inserted between the NcoI and SacI, and the SacI and HindIII sites of the pET28a(+) vector with a GGGSGGGS linker between them. In tandem constructs, all mutations were introduced into the KirBac1.1 monomer plasmid by a site-directed mutagenesis kit (Agilent) and were then subcloned into the tandem dimer or tetramer constructs. A $His_8$ tag was introduced in the C termini of all the protomers for metal affinity purification.

**Protein expression and purification.** KirBac1.1 WT protein was expressed in the BL21-Gold(DE3)-pLysS host strain, after induction by 1.0 mM IPTG for 3 h at 37 °C, when the $OD_{600}$ had reached ~0.8–1.0. KirBac1.1 tandem dimer or tetramer constructs were expressed in the BL21-Gold(DE3) host strain, and cultures were induced by 0.1 mM IPTG overnight at 20 °C when the $OD_{600}$ reached about ~0.6–0.8. Metal affinity purification was performed as previously described[43,44]. Affinity-purified proteins were loaded onto a gel-filtration column (Superdex-200, GE Healthcare), and tetramer fractions were collected for the following functional or structural studies.

**Protein labeling.** Tetramer fractions of KirBac1.1 proteins were concentrated to 1 mg/ml in labeling buffer containing 20 mM HEPES, 150 mM KCl, and 5 mM DM, pH 7.0. A 1:1 mixture of Alexa Fluor 555 and 647 c2 maleimide were added into the protein solution at protein/fluorophore ratio of 1:4. Labeling reactions were conducted at room temperature for 2 h, terminated by 10 mM β-mercaptoethanol and then incubated at room temperature for an additional 30 min. Labeled proteins were diluted 10× in labeling buffer and then mixed with cobalt affinity resin (Clontech). Free fluorophores were completely removed by extensive washing (>100 bed volumes), and protein was eluted by elution buffer (20 mM HEPES, 150 mM KCl, 5 mM DM, and 400 mM imidazole, pH 7.5). Eluted proteins were loaded on a gel-filtration column (Superdex-200 10/30, GE Healthcare), and tetramer fractions were collected and concentrated for rubidium flux assay or single-molecule imaging experiments.

**Rubidium flux assay.** Purified KirBac1.1 proteins were reconstituted into POPE/POPG (3:1) liposomes with or without 1% (w/w) $PIP_2$, at a protein/lipid ratio of 1:100. The protein and lipid mixtures were incubated for 20 min at room temperature, and proteoliposomes were formed by removing the detergent with Sephadex G-50 spin columns. Rubidium flux assays were performed on proteoliposome samples as previously described[22,44]. Rubidium uptake of all mutants was normalized against that of WT protein in liposomes without $PIP_2$. We used purified brain $PIP_2$ (Avanti 840046P), which was mixed with either K-MOPS buffer for rubidium flux assays and single-channel recordings or K-HEPES-Trolox buffer for single-molecule imaging with the final predicted nominal concentration of 5 or 100 μM. $PIP_2$ probably assembles into micelles and then incorporates into liposomes by micelle fusion, at which point it cannot be washed away.

**Single-channel recordings.** Single-channel recordings were performed on reconstituted WT KirBac1.1 in giant liposomes as previously described[20]. Excised inside-out patch recordings were performed with electrodes of 2–5 MΩ and symmetrical bath and pipette solutions consisting of 20 mM MOPS and 158 mM KCl and adjusted to pH 7.5 (KOH). Single-channel current responses were measured at an applied membrane potential of −100 mV, amplified and low pass–filtered at 1 kHz, sampled at 10 kHz (Axopatch 1B, 4-pole Bessel), converted into digital files in Clampex7, and stored on an external hard drive for offline analysis with QuB kinetic software (http://www.qub.buffalo.edu/).

**Single-molecule Imaging.** KirBac1.1 tandem proteins labeled with Alexa Fluor 555 and Alexa Fluor 647 were mixed with lipids (10 mg/ml, POPE/POPG (3:1) and 2% biotinylated POPE, in buffer containing 20 mM HEPES, 150 mM KCl, 1 mM EDTA, 1 mM EGTA, and 35 mM CHAPS, pH 7.5) at a protein/lipid ratio of 1:200 (w/w). The mixtures were incubated for 20 min at room temperature, and proteoliposomes were formed by removing the detergent with Sephadex G-50 spin columns. Proteoliposomes were diluted 10–50 times with reconstitution buffer (20 mM HEPES, 150 mM KCl, 1 mM EDTA, and 1 mM EGTA, pH 7.5), loaded into a PEGylated sample chamber and immobilized on the surface through neutravidin[45]. Single-molecule imaging was performed on a prism-based TIRF microscope with a 532-nm laser as excitation light. At the beginning or end of single-molecule imaging, 640-nm excitation was also used to confirm the existence of acceptor fluorophore, particularly for constructs with low FRET efficiencies. The imaging buffer contained 20 mM HEPES, 150 mM KCl, 1 mM EDTA, 1 mM EGTA, ~3 mM Trolox, 1 mM 4-nitrobenzyl alcohol (NBA) and 1 mM cyclooctatetraene (COT), pH 7.5. After collection of single-molecule imaging data in control conditions (without $PIP_2$), the imaging buffer was replaced with $PIP_2$-containing buffer (imaging buffer with an additional 100 μM $PIP_2$). After 5 min of incubation, the sample chamber was flushed again with $PIP_2$ imaging buffer, and then single-molecule images were collected according to the same procedure as that for control conditions.

**Data analysis.** *Single-channel recordings.* Preprocessing and analyses of single-channel current recordings were performed offline with QuB software (http://www.qub.buffalo.edu/). Brief (fewer than nine samples) current spikes during prolonged closures were adjusted to the adjacent nonconducting current amplitude to eliminate infrequent electrical noise, and instances of baseline drift were corrected by setting the baseline to an initial zero-current level through the use of baseline nodes. Current amplitudes were estimated from preprocessed data with the 'AMP' function, which uses the Baum-Welch reestimation algorithm and were typically well described by three Gaussian components corresponding to one nonconducting and two resolvable conducting amplitudes. Whole file recordings were digitally low pass–filtered at 400 Hz and idealized with a 50% threshold method using the corresponding single-channel amplitudes with no imposed dead time. The resulting idealization was inspected by visual comparison to that of the digitally filtered current signal. Interval distributions were typically well fit with three closed components and one open component for each open conductance class.

*Single-molecule FRET data analysis.* The movies acquired in single-molecule imaging were processed with an IDL script (available on request) to identify and extract donor and acceptor fluorescence intensity profiles of individual molecules[28]. Traces extracted from the movies were interactively selected, with the following acceptance criteria: (i) no more than one bleaching step for both donor and acceptor fluorophores; (ii) donor and acceptor fluorescence intensities showing a clear anticorrelated pattern; (iii) constant total fluorescence intensity from donor and acceptor before photobleaching; (iv) lifetimes of both donor and acceptor fluorophore longer than 5s. All analyzed smFRET traces were selected independently by two analysts (S.W. and R.V.) and then were analyzed with the same algorithm. No significant difference were found between the traces selected by S.W. and R.V.

The bin size of all histograms was set as 0.02. FRET histograms of each single trace, regardless of length, were normalized to total counts (i.e., every trace contributed equally to the final histograms, to avoid dominant effects of long traces). The final histograms were obtained by combining the FRET histograms of each trace and then renormalizing against total counts. To generate FRET contour plots, the first 5 s of data from each trace were extracted, and the histogram at each time point was obtained and normalized to total counts. The normalized coefficients of cross-correlation were calculated with the 'xcov' function (Signal Processing Toolbox) in Matlab. The maximum lag was 20 s, and traces shorter than 20 s were excluded from the analysis. The cross-correlation data were fitted with a two-component exponential function with the curve-fitting tool box in Matlab. Calculated time constants and areas for individual exponential components were tabulated and reported as means ± s.e.m.


43. Enkvetchakul, D. *et al.* Functional characterization of a prokaryotic Kir channel. *J. Biol. Chem.* **279**, 47076–47080 (2004).
44. Wang, S., Alimi, Y., Tong, A., Nichols, C.G. & Enkvetchakul, D. Differential roles of blocking ions in KirBac1.1 tetramer stability. *J. Biol. Chem.* **284**, 2854–2860 (2009).
45. Joo, C. & Ha, T. Preparing sample chambers for single-molecule FRET. *Cold Spring Harb. Protoc.* **2012**, 1104–1108 (2012).